nature materials

LETTERS

PUBLISHED ONLINE: 13 FEBRUARY 2017 | DOI: 10.1038/NMAT4840

Universal lower limit on vortex creep in superconductors

S. Eley[1]*, M. Miura[2], B. Maiorov[1] and L. Civale[1]

Superconductors are excellent testbeds for studying vortices, topological excitations that also appear in superfluids, liquid crystals and Bose–Einstein condensates. Vortex motion can be disruptive; it can cause phase transitions[1], glitches in pulsars[2], and losses in superconducting microwave circuits[3], and it limits the current-carrying capacity of superconductors[4]. Understanding vortex dynamics is fundamentally and technologically important, and the competition between thermal energy and energy barriers defined by material disorder is not completely understood. Specifically, early measurements of thermally activated vortex motion (creep) in iron-based superconductors unveiled fast rates (S) comparable to measurements of $YBa_2Cu_3O_{7-\delta}$ (refs 5–10). This was puzzling because S is thought to somehow correlate with the Ginzburg number (Gi), and Gi is significantly lower in most iron-based superconductors than in $YBa_2Cu_3O_{7-\delta}$. Here, we report very slow creep in $BaFe_2(As_{0.67}P_{0.33})_2$ films, and propose the existence of a universal minimum realizable $S \sim Gi^{1/2}(T/T_c)$ (T_c is the superconducting transition temperature) that has been achieved in our films and few other materials, and is violated by none. This limitation provides new clues about designing materials with slow creep and the interplay between material parameters and vortex dynamics.

The search for a universal description of vortex matter—one that is applicable to a range of systems and regimes—is a formidable challenge, complicated by the complexity of the interactions between vortices and the environment. Vortex motion that can be induced by Magnus and Lorentz forces or thermal activation can also be counteracted by pinning forces. As vortex cores are normal (that is, superfluidity or superconductivity is destroyed inside them), creating a vortex costs energy, and pinning can occur when it is energetically more favourable for a vortex to appear in one location than in another. In type-II superconductors at high enough magnetic fields, vortices are formed by the penetration of magnetic flux, and material disorder that locally reduces the vortex core energy can produce pinning forces that almost completely preclude vortex motion. This results in nearly zero resistance, as long as the current density (J) does not exceed the critical current density (J_c). The caveat is that, for $J < J_c$, vortices are in metastable states inside pinning centres that act as finite potential wells, and thermal fluctuations may enable them to jump out (creep). Creep is seldom problematic in applications involving low-T_c superconductors (LTS), which typically exhibit slow creep (the decay over time in the persistent current, $S = |(d\ln J)/(d\ln t)|$). Consequently, Nb–Ti solenoids in magnetic resonance imaging systems can operate in 'persistent mode', retaining the field for essentially indefinite time frames. However, creep is fast in high-T_c superconductors (HTS), restricting applications and reducing the effective J_c.

Superconductors are ideal for studying fundamental questions regarding vortex dynamics because vortex motion introduces easily measurable dissipation into these materials. Furthermore, we can tune the strength of interactions between vortices and the potential energy landscape by incorporating pinning centres (for example, secondary phases[4] such as $BaZrO_3$) or comparing materials with different properties (different Gi). The Ginzburg number, $Gi = \left(\gamma^2/2\right)\left[(\mu_0 k_B T_c)/\left(4\pi B_c^2(0)\,\xi_{ab}^3(0)\right)\right]^2 \propto \gamma^2 T_c^2 \lambda^4/\xi^2$, parameterizes the scale of thermal fluctuations in a superconductor[11]; γ is the electronic mass anisotropy, $B_c(T=0) = \Phi_0/(2\sqrt{2}\pi\lambda_{ab}(0)\xi_{ab}(0))$ is the thermodynamic critical field, Φ_0 is the flux quantum, $\xi_{ab}(T=0)$ is the coherence length, and $\lambda_{ab}(T=0)$ is the penetration depth. As Gi in $YBa_2Cu_3O_{7-\delta}$ (YBCO) is orders of magnitude larger than in Nb–Ti ($\sim 10^{-2}$ and 10^{-8}, respectively), it is universally accepted that this difference roughly accounts for the much faster creep in YBCO[11]. The same considerations suggest that iron-based superconductors (Fe-SCs) should have creep rates between those of LTS and HTS, but this is not what was observed. The exceptionally fast creep in many Fe-SCs[5–10] not only eludes conventional wisdom, but also stymies application. This problem highlights an important, yet unresolved, challenge: can we predict $S(T)$ in any material?

To investigate the creep problem in Fe-SCs, we chose to study $BaFe_2(As_{0.67}P_{0.33})_2$ because there is evidence of a strong pinning landscape in this material, demonstrated by high J_c (ref. 12), that can be further enhanced by introducing $BaZrO_3$ (BZO) nanoparticles[13] (Fig. 1). In fact, the force exerted by the pinning landscape in films containing BZO rivals that in MgB_2, NbTi and Nb_3Sn[13]. It has an intermediate $Gi \approx 8.6 \times 10^{-5}$, calculated using $\gamma = 1.55$ (ref. 13), $\lambda_{ab}(T=0) \approx 185$ nm (see Supplementary Information), and $\xi_{ab}(T=0) \approx \sqrt{\Phi_0/2\pi\mu_0 H_{c2}(0)} \approx 2.5$ nm (ref. 14). Here, we compare results for two 80-nm-thick $BaFe_2(As_{0.67}P_{0.33})_2$ films grown by pulsed laser deposition on MgO substrates[13], one containing a uniform dispersion of BZO nanoparticles (Ba122:P+BZO) and one without (Ba122:P).

Magnetization ($M \propto J_c$) studies were performed in a superconducting quantum interference device magnetometer (see Methods). By recording successive measurements of M every 15 s for an hour, at different temperatures (T) and fields (H), we capture the logarithmic decay over time in J and determine both $J_c(T,H)$ and $S(T,H)$. We see that the nanoparticles increase J_c(5K, 200 Oe) by only ~12% and that this enhancement vanishes at high T (Fig. 1b), but increases dramatically with increasing field (400% at 2 T, Fig. 1c). This field-dependent enhancement in J_c is not surprising. Similar to defects created by particle irradiation[4,15], the efficacy of the BZO in immobilizing vortices is magnified as the number of vortices approaches the number of available pinning sites. Consistent with other studies[12,13,16,17], J_c is also high in films without nanoparticles. Strong pinning in this material has been ascribed to spatial

[1]Condensed Matter and Magnet Science, Los Alamos National Laboratory, Los Alamos, New Mexico 87545, USA. [2]Graduate School of Science and Technology, Seikei University, 3-3-1 Kichijoji-Kitamachi, Musashino-shi, Tokyo 180-8633, Japan. *e-mail: seley@lanl.gov

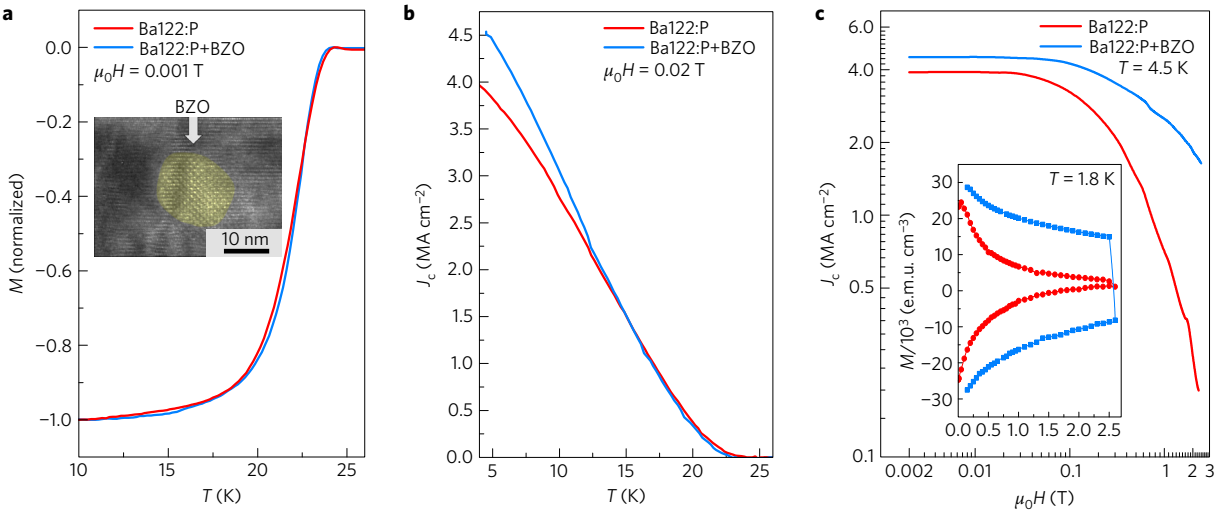

Figure 1 | Enhancement in the critical current of $BaFe_2(As_{0.67}P_{0.33})_2$ films with the addition of $BaZrO_3$ (BZO) nanoparticles. a,**b**, Comparison of the temperature dependence of the magnetization (M) at $\mu_0H = 0.001$ T (**a**) and critical current density (J_c) at $\mu_0H = 0.02$ T (**b**) in Ba122:P and Ba122:P+BZO. The BZO nanoparticles are ~8 nm in diameter and spaced 24 nm apart (that is, density of 6.8×10^{22} m^{-3}). The addition of nanoparticles does not degrade the critical temperature, $T_c \approx 24.7$ K. The inset to **a** is a cross-sectional high-resolution transmission electron microscopy image of the Ba122:P+BZO film, in which a BZO nanoparticle can be easily discerned. **c**, Field dependence of J_c at $T = 4.5$ K and (inset) magnetization at $T = 1.8$ K.

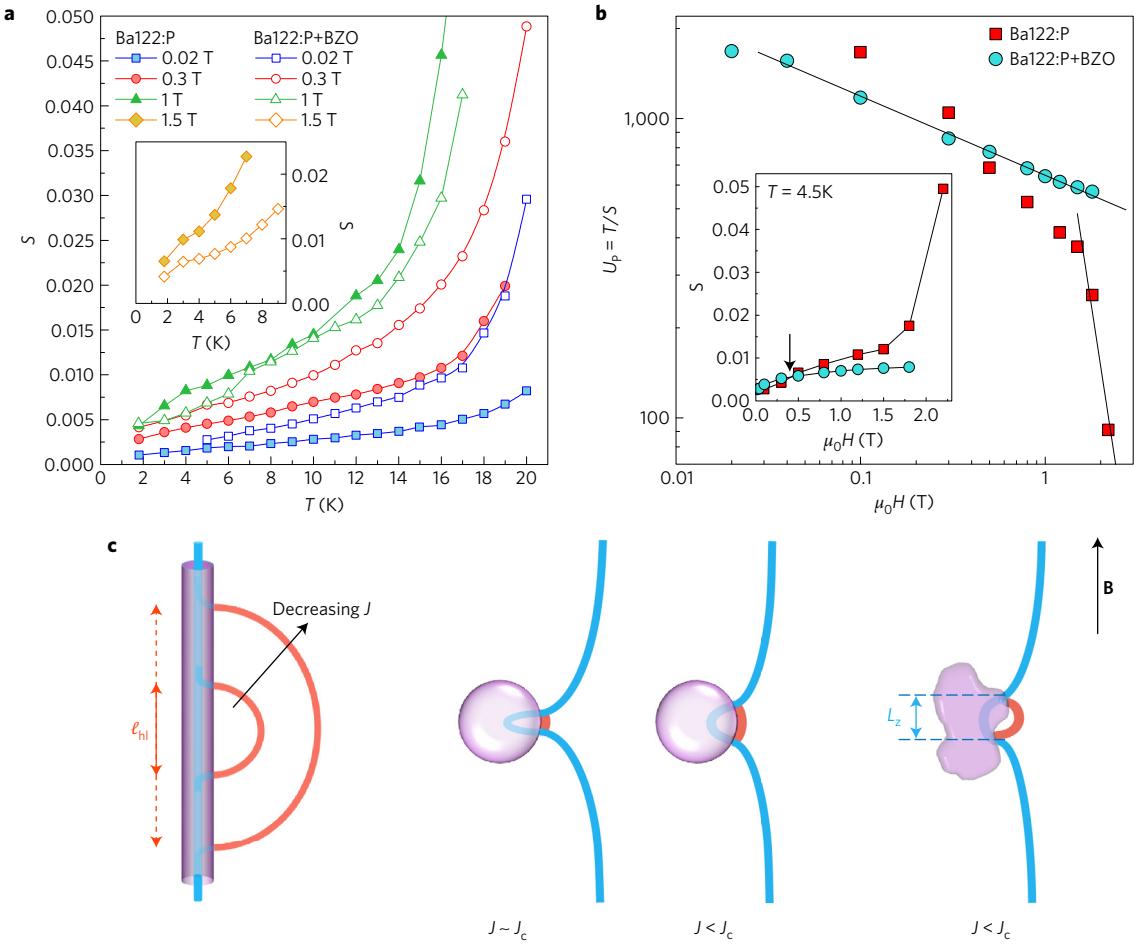

Figure 2 | Temperature and field dependence of creep. a, Comparison of the temperature-dependent creep rate, $S(T)$, in Ba122:P and Ba122:P+BZO at $\mu_0H = 0.02$ T, 0.3 T, 1 T and (inset) 1.5 T. **b**, Comparison of field-dependent activation energies, $U_P = T/S$, and (inset) creep at $T = 4.5$ K in both samples. The BZO nanoparticles become effective in lowering creep in high fields $\mu_0H \geq 0.5$ T; the crossover is noted by the arrow in the inset. **c**, Illustration of excitations of a vortex line from a columnar defect, spherical nanoparticle (in the early, then later, stages of relaxation), and nanoparticle of arbitrary shape through half-loop formation. Thermal excitations can cause vortex lines (blue curves) pinned to defects (purple shapes) to form half-loops (red curves), leading to creep. The size of the loop grows as the depinning process progresses with time (current density J decreases). Here, L_z is the length of the pinned core and ℓ_{hl} represents the half-loop length, both measured along the direction of the field (**B**).

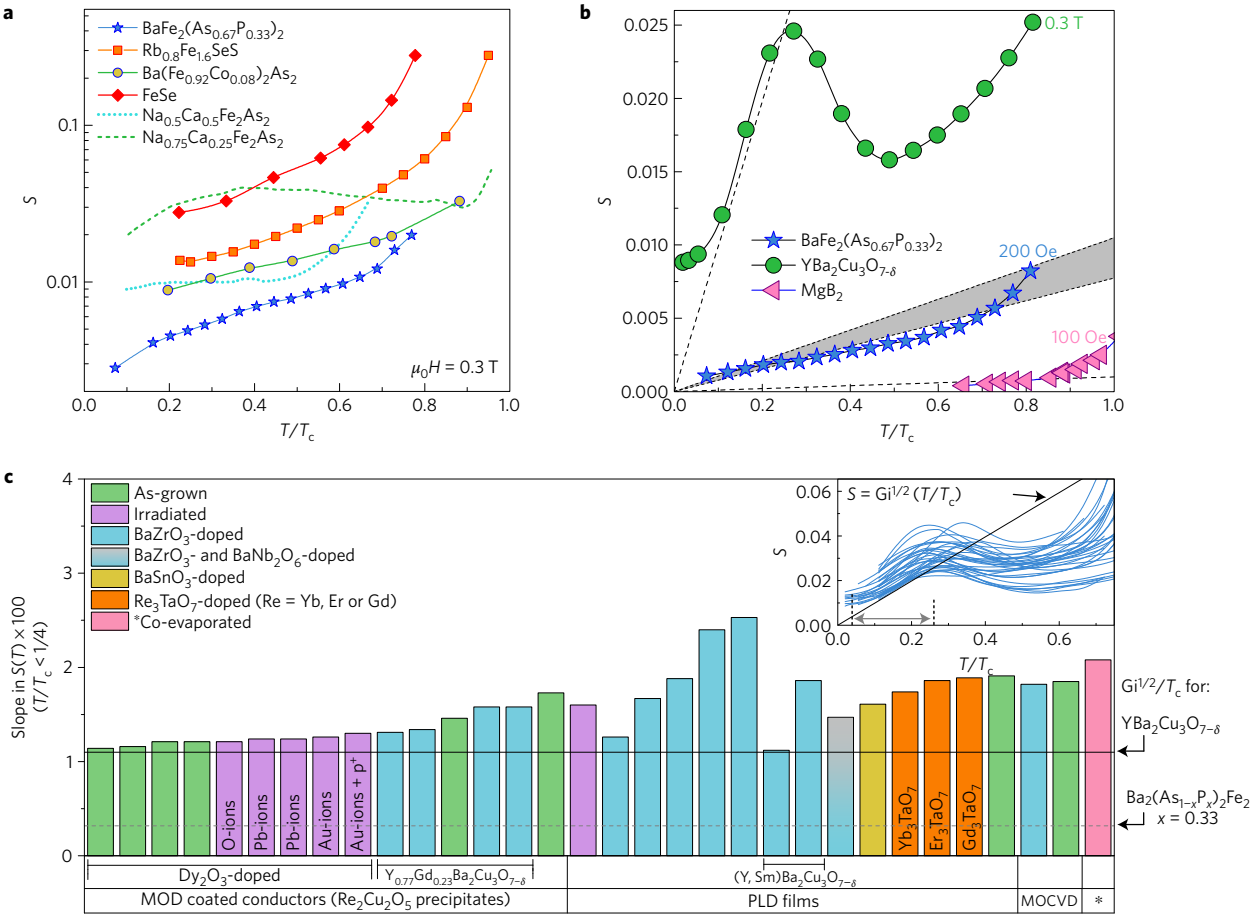

Figure 3 | Creep in iron-based superconductors, MgB_2 and $YBa_2Cu_3O_{7-\delta}$. a, A comparison of creep versus reduced temperature, $S(T/T_c)$, in different iron-based superconductors, where the data for FeSe were extracted from $S(H)$ at different temperatures[9], $Ba(Fe_{0.92}Co_{0.08})_2As_2$ was irradiated[20], the data from $Na_{1-x}Ca_xFe_2As_2$ are from ref. 8, we measured $Rb_{0.8}Fe_{1.6}SeS$ (J. Yang, S.E., D. Wulferding, V. Tsurkan, L.C. and J. Kim, manuscript in preparation), and $BaFe_2(As_{0.67}P_{0.33})_2$ is the Ba122:P film from this study. All previous studies of creep in iron-based superconductors have been performed on single crystals[5–8,10,15,20,31,32] where self-fields ($H_{sf} \propto J_c \times$ thickness) are higher than in our films. Consequently, we perform a direct comparison at $\mu_0H = 0.3$ T because it is higher than self-field in all samples, is a relatively low field, which typically results in lower $S(T)$ than higher fields, and was a common choice in available data. **b**, $S(T/T_c)$ at the indicated fields (lowest field used that is above self-field) in a $BaFe_2(As_{0.67}P_{0.33})_2$ (Ba122:P) film, a $YBa_2Cu_3O_{7-\delta}$-coated conductor[33], and an MgB_2 (ref. 28) film. The limit set by $Gi^{1/2}T/T_c$ is shown for each respective film by the dashed lines. The grey region captures the uncertainty in $Gi^{1/2}T/T_c$, due to the uncertainty in λ (170 nm from μSr measurements and 200 nm from measurements using a tunnel-diode oscillator[14]) for Ba122:P. **c**, The histogram shows the slope in S versus T at $\mu_0H = 0.3$ T for $YBa_2Cu_3O_{7-\delta}$ (or, if specified, $Y_{1-x}Re_xBa_2Cu_3O_{7-\delta}$, where Re=Gd or Sm) samples with a wide range of pinning landscapes (see Supplementary Information) for films grown by metal-organic deposition (MOD), pulsed laser deposition (PLD), metal-organic chemical vapour deposition (MOCVD), or co-evaporation. The inset shows the raw data. The slope was extracted for $T/T_c \leq 1/4$ (Anderson–Kim regime for these samples, indicated by the grey double-headed arrow) and quantum creep is not considered (the fit is forced through $T = 0$, $S = 0$).

variations in the P dopant concentration[12,16]. Namely, the T_c and ξ in $BaFe_2(As_{1-x}P_x)_2$ are exceptionally sensitive to the stoichiometry[17], such that these variations demarcate phase-separated regions that are effective pinning sites. These regions are spaced roughly 100 nm apart[16], and, therefore, outnumber the vortices in fields less than $B_\phi \sim 2\Phi_0/\sqrt{3}a_0^2 \approx 0.2$ T. This is analogous to pinning in $Sm_{1+x}Ba_{2-x}Cu_3O_y$ (Sm123) films, in which Sm-rich123 precipitates of lower T_c than the Sm123 matrix are effective pinning centres[18].

Figure 2a shows $S(T)$ at different fields for both films, revealing behaviour consistent with the Anderson–Kim model. A defect (or collection of defects) pins a vortex segment (or a bundle of vortices) by reducing the vortex line energy by the pinning energy, $U_p(T,H)$. The current-induced force reduces U_p to an activation energy $U_{act}(T, H, J)$, so the vortex hopping rate is proportional to $e^{-U_{act}/T}$. All of the complexity of the creep phenomenon is contained in $U_{act}(T, H, J)$. The Anderson–Kim model assumes $U_{act}(J) \propto U_P|1 - J/J_c|$, such that $S(T) \approx k_BT/U_P(T)$ (ref. 11). For $T \ll T_c$, $U_p(T)$ is approximately constant and S increases linearly with T; at higher temperatures, $S(T)$ steepens as $U_p(T)$ decreases. The data in Fig. 2a are well described by this scenario, except that the curves extrapolate to non-zero values as T extrapolates to zero, indicative of a measurable contribution from quantum creep (a non-thermal, tunnelling process)[11].

Comparing $S(T)$ in both films (Fig. 2a), we see that the addition of BZO increases S for $\mu_0H = 200$ Oe and 0.3 T. Hence, BZO nanoparticles counteract the strong pinning effects of the large pre-existing phase-separated regions. To understand this, note that in the Ba122:P+BZO film, vortices will pin to both the sparse phase-separated regions and the BZO. The BZO nanoparticles are presumably smaller than the phase-separated regions, and, therefore, have lower U_p such that vortices pinned to them will have higher S. At low fields (that is, fewer vortices than phase-separated regions), we find overall higher S for the Ba122:P+BZO film. The situation reverses at high fields. From Fig. 2a, we see that at $\mu_0H \geq 1$ T, the film with nanoparticles shows slower $S(T)$ and, from Fig. 2b (inset), that this crossover occurs around $\mu_0H = 0.5$ T at $T = 4.5$ K. Thus,

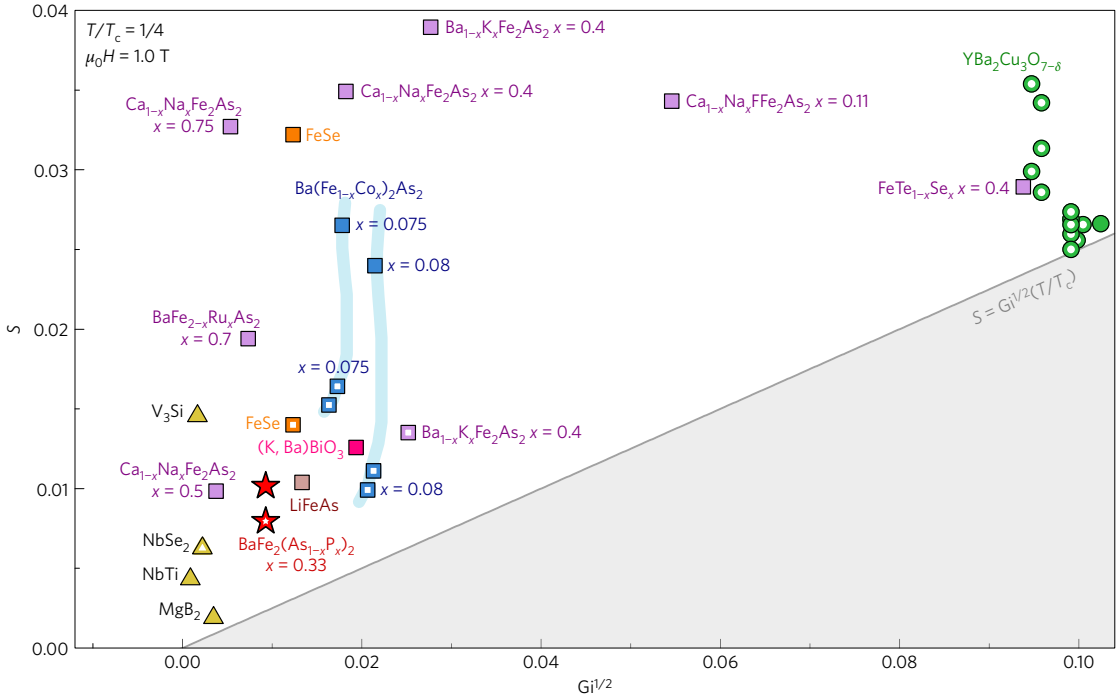

Figure 4 | The universal lower limit for creep. Creep at reduced temperature $T/T_c = 1/4$ and field of $\mu_0 H = 1$T for different superconductors plotted versus $Gi^{1/2}$. See Supplementary Tables 1–3 for more details and Supplementary Fig. 1 for a similar comparison at $\mu_0 H = 0.3$T. The open symbols indicate materials for which the microstructure has been modified by either irradiation or incorporation of inclusions. The solid grey line represents the limit set by $Gi^{1/2}T/T_c = Gi^{1/2}/4$. We have chosen $T = T_c/4$ because it is a low temperature where the Anderson–Kim description is typically valid, and $\mu_0 H = 1$T because it is the lowest field for which a large amount of S data is available in the literature. By connecting the data for $Ba(Fe_{1-x}Co_x)_2As_2$ ($x = 0.075$ and $x = 0.08$) collected before and after two different irradiation processes, the broad blue lines highlight examples of samples for which systematic modifications of the microstructure have tuned S towards the limit.

above this field, the vortex population is high enough that BZO becomes effective in slowing creep as it offers more pinning sites to immobilize a higher fraction of vortices than the Ba122:P film.

From comparing our results with other studies, we find that creep in the Ba122:P film is not only remarkably slow, but is in fact the slowest measured creep rate in any Fe-SC to date (Fig. 3a). Prior to this study, we had speculated that creep for other Fe-SCs seemed surprisingly fast[5–10], which raised an important question: precisely what should we expect and how much lower can we go?

Gi dictates various properties, including the width of the critical fluctuation region around T_c (that is, $\Delta T_c \sim GiT_c$, setting the lower limit for the superconducting transition width for a crystallographically perfect sample) and the vortex melting transition[11,19]. It is known that Gi will impact S and it has become perfunctory to mention an estimate of Gi (refs 6,20–23) when characterizing vortex dynamics, but a testable formula has not been developed. In pursuit of such a formula, we now review how vortices depin from various pinning centres (applicable to crystals, films, devices and wires). We restrict ourselves to the early stages of the depinning process ($J \sim J_c$), low T (where U_p is nearly temperature independent) and low H (single-vortex regime (sv)). Vortex lines can be pinned either by the collective action of many weak pins or the independent action of strong pins[24]. First considering the most pervasive defect, point defects are weak pins that will provide sufficient pinning only when acting collectively. Here, $J_c \equiv J_{sv}$ is highest and the pinning energy is given by[11] $U_P \equiv U_{sv} \sim H_c^2\left(\xi_{ab}^3/\gamma\right)(J_{sv}/J_0)^{1/2}$, where J_0 is the depairing current density, the theoretically maximum achievable J_c. Consequently, the resulting creep rate is $S \sim T/U_P \sim \sqrt{2}\,(J_0/J_{sv})^{1/2}\,Gi^{1/2}\,(T/T_c)$, so the scale of S depends on $Gi^{1/2}$. The prefactor $(J_0/J_{sv})^{1/2} > 1$ decreases as J_{sv} increases, but in practice $J_{sv} \ll J_0$, thus $S > Gi^{1/2}\,(T/T_c)$.

Now consider a single vortex trapped by a strong individual pinning centre, $U_P(T) \sim (H_c^2/8\pi)V_P$, where V_p is the volume of the vortex core that is pinned. Strong pinning can occur in defects of dimensions $\sim\xi$ or larger. For an insulating inclusion of size equal to the coherence volume, that is, an ellipsoid of semi axes ξ_{ab} and $\xi_c = \xi_{ab}/\gamma$ such that $V_P \equiv V_{coh} \sim (4\pi/3)\xi_{ab}^3/\gamma$, we obtain $U_P \equiv U_{coh} \sim H_c^2\xi_{ab}^3/6\gamma$; thus, in the Anderson–Kim regime, $S \sim (T/U_P) \sim 6\sqrt{2}Gi^{1/2}(T/T_c)$, once again proportional to $Gi^{1/2}$.

The obvious strategy to minimize S is to increase U_p by increasing the length of the core that is pinned. For a defect of dimensions bigger than ξ and arbitrary shape, $V_P \sim 2\pi\xi_{ab}^2 L_z \sim (3/2)\,(L_z/\xi_c)\,V_{coh}$, where $L_z > \xi_c$ is the size along the field direction (see Fig. 2c) and $\sqrt{2}\xi$ is the vortex core radius. There is, however, a limit to this approach set by the elastic properties of vortex matter, which are not considered by the Anderson–Kim model. This can be easily visualized by considering a vortex pinned in a columnar defect, from which it can depin by producing a half-loop of length $\ell_{hl} \sim \xi_c(J_0/J)$ along the columnar defect (Fig. 2c). Even for an arbitrarily long columnar defect, the effective L_z is truncated by ℓ_{hl} so $V_P \sim 2\pi\xi_{ab}^2\ell_{hl}$. For $J \sim J_c$, the activation energy $U_{act}(J) \sim (4\pi/\gamma)H_c^2\xi_{ab}^3(J_0/J_c)(1-J/J_c)$ (ref. 25) resulting in $S \sim 4\sqrt{2}(J_c/J_0)Gi^{1/2}(T/T_c)$.

For randomly distributed nanoparticles of radius $R \gg \xi(T=0)$, with increasing J the tips of the pinned vortex slide along the surface of the nanoparticle until they meet near the equator and reconnect, leading to depinning of the vortex[26] (Fig. 2c). As J decays during relaxation, the two tips progressively separate. While $J \sim J_c$, the separation is small and a thermal fluctuation that creates a short vortex segment that connects the tips is enough to depin the vortex; thus, U_{act} is small and S is large regardless of R. The length of the segment required for a depinning fluctuation increases with decreasing J, resembling the case of a columnar defect where $L_z \sim 2R$. If R is very large and the energy of creating a segment connecting both tips becomes too large, depinning may occur through the creation of a localized excitation analogous to

a half-loop from a columnar defect, and the above estimate for S is recovered. The argument can be extended to large defects of arbitrary shape and, while the numerical details may be system-dependent, a relation of the form $S \sim A^* \mathrm{Gi}^{1/2}(T/T_c)$, where A is an unknown proportionality constant, will still hold.

To estimate A, we start with $A \sim 4\sqrt{2}(J_c/J_0)$ for a columnar defect. In systems with vortex-dominated dissipation, a maximum of $J_c/J_0 \sim 0.2$–0.25 (ref. 27) has been achieved, so $A \sim 1$. For defects of diverse morphology, we obtain an estimate for A empirically using a wealth of $S(T)$ data from YBCO samples with different microstructures (Fig. 3c) and see that again $A \sim 1$. Thus, we conclude that, at low temperature (where U_p is nearly temperature independent) and low field (where vortex–vortex interactions are negligible), $S(T)$ cannot be significantly smaller than $S \sim \mathrm{Gi}^{1/2}(T/T_c)$ for $J \sim J_c$ (see Supplementary Information for further discussion). This reveals a fundamental limitation to how much creep can be slowed through modifications of the microstructure, and can serve as a guide for when further improvements can be achieved. In light of this, we find that S in our films has the same relationship to Gi as we found in the YBCO films with the slowest creep, and that our films have reached the slowest creep allowed by Gi.

By compiling results from the literature for different superconductors, we reveal a cogent picture of this limitation and find few materials, including our Ba122:P film, MgB_2 (refs 28,29) and YBCO, with measured creep rates near our proposed limit (Fig. 3b). Figure 4 shows $S(T = T_c/4, \mu_0 H = 1\,\mathrm{T})$ for many materials covering a broad range of values for Gi. The straight line at $S \sim \mathrm{Gi}^{1/2}/4$ demarcates a region of unobtainable S values; strikingly, no data appear below it. This hard constraint, which had not been established until now, has two broad implications: first, the creep problem in HTS cannot be fully eliminated and there is a limit to how much it can be ameliorated, and secondly, we can confidently predict that any yet-to-be-discovered HTS will have fast creep. Additionally, these results will help in designing materials for superconducting devices, wires and magnets, and could provide insight on open questions in other systems in which topological excitations undergo depinning processes, for example, skyrmions in magnetic films[30].

Methods

Methods, including statements of data availability and any associated accession codes and references, are available in the online version of this paper.

Received 20 July 2016; accepted 29 November 2016; published online 13 February 2017

References

1. Lin, S.-Z. *et al*. Topological defects as relics of emergent continuous symmetry and Higgs condensation of disorder in ferroelectrics. *Nat. Phys.* **10,** 970–977 (2014).
2. Kawaler, S. D., Novikow, I. & Srinivasan, G. *Stellar Remnants* (Springer-Verlag, 1995).
3. Song, C., Defeo, M. P., Yu, K. & Plourde, B. L. T. Reducing microwave loss in superconducting resonators due to trapped vortices. *Appl. Phys. Lett.* **95,** 232501 (2009).
4. Foltyn, S. R. *et al*. Materials science challenges for high-temperature superconducting wire. *Nat. Mater.* **6,** 631–642 (2007).
5. Sun, Y. *et al*. Magnetic relaxation and collective vortex creep in $FeTe_{0.6}Se_{0.4}$ single crystal. *Europhys. Lett.* **103,** 57013 (2013).
6. Haberkorn, N., Eom, M. J., You, J. S., Kim, J. & Kim, J. S. Critical current densities and flux creep rates in near optimally doped $BaFe_{2-x}Ru_xAs_2$ ($x \approx 0.7$) single crystals. *Solid State Commun.* **231–232,** 26–30 (2016).
7. Shlyk, L. *et al*. Crystal structure and superconducting properties of hole-doped $Ca_{0.89}Na_{0.11}FFeAs$ single crystals. *Supercond. Sci. Technol.* **27,** 044011 (2014).
8. Haberkorn, N. *et al*. Strong pinning and elastic to plastic vortex crossover in Na-doped $CaFe_2As_2$ single crystals. *Phys. Rev. B* **84,** 094522 (2011).
9. Sun, Y. *et al*. Critical current density, vortex dynamics, and phase diagram of single-crystal FeSe. *Phys. Rev. B* **92,** 144509 (2015).
10. Sun, Y. *et al*. Enhancement of critical current density and mechanism of vortex pinning in H^+-irradiated FeSe single crystal. *Appl. Phys. Express* **8,** 113102 (2015).
11. Blatter, G., Feigel'man, M. V., Geshkenbein, V. B., Larkin, A. I. & Vinokur, V. M. Vortices in high-temperature superconductors. *Rev. Mod. Phys.* **66,** 1125–1388 (1994).
12. Kurth, F. *et al*. Unusually high critical current of clean P-doped $BaFe_2As_2$ single crystalline thin film. *Appl. Phys. Lett.* **106,** 072602 (2015).
13. Miura, M. *et al*. Strongly enhanced flux pinning in one-step deposition of $BaFe(As_{0.66}P_{0.33})_2$ superconductor films with uniformly dispersed $BaZrO_3$ nanoparticles. *Nat. Commun.* **4,** 2499 (2013).
14. Hashimoto, K. *et al*. Line nodes in the energy gap of superconducting $BaFe_2(As_{1-x}P_x)_2$. *Phys. Rev. B* **81,** 220501 (2010).
15. Tamegai, T. *et al*. Effects of particle irradiations on vortex states in iron-based superconductors. *Supercond. Sci. Technol.* **25,** 084008 (2012).
16. Demirdis, S. *et al*. Disorder, critical currents, and vortex pinning energies in isovalently substituted $BaFe_2(As_{1-x}P_x)_2$. *Phys. Rev. B* **87,** 094506 (2013).
17. Miura, M. *et al*. Anisotropy and superconducting properties of $BaFe_2(As_{1-x}P_x)_2$ films with various phosphorus contents. *Appl. Phys. Express* **6,** 93101 (2013).
18. Awaji, S. *et al*. J_c and B_i properties of $Sm_{1+x}Ba_{2-x}Cu_3O_y$ films with nano-particles. *Physica C* **463–465,** 669–673 (2007).
19. Bennemann, K.-H. & Ketterson, J. B. *Superconductivity: Volume 1: Conventional and Unconventional Superconductors* (Springer Science & Business Media, 2008).
20. Haberkorn, N. *et al*. Enhancement of the critical current density by increasing the collective pinning energy in heavy ion irradiated Co-doped $BaFe_2As_2$ single crystals. *Supercond. Sci. Technol.* **28,** 055011 (2015).
21. Hänisch, J. *et al*. High field superconducting properties of $Ba(Fe_{1-x}Co_x)_2As_2$ thin films. *Sci. Rep.* **5,** 17363 (2015).
22. Zehetmayer, M. How the vortex lattice of a superconductor becomes disordered: a study by scanning tunneling spectroscopy. *Sci. Rep.* **5,** 09244 (2015).
23. Gurevich, A. Iron-based superconductors at high magnetic fields. *Rep. Prog. Phys.* **74,** 124501 (2011).
24. Blatter, G., Geshkenbein, V. B. & Koopmann, J. A. G. Weak to strong pinning crossover. *Phys. Rev. Lett.* **92,** 067009 (2004).
25. Malozemoff, A. P. & Fisher, M. P. A. Universality in the current decay and flux creep of Y–Ba–Cu–O high-temperature superconductors. *Phys. Rev. B* **42,** 6784–6786 (1990).
26. Koshelev, A. E. & Kolton, A. B. Theory and simulations on strong pinning of vortex lines by nanoparticles. *Phys. Rev. B* **84,** 104528 (2011).
27. Wimbush, S. *Applied Superconductivity: Handbook on Devices and Applications, Volume 1* (Wiley, 2015).
28. Kim, J. *et al*. Strong magnetic field dependence of critical current densities and vortex activation energies in an anisotropic clean MgB_2 thin film. *Solid State Commun.* **204,** 56–60 (2014).
29. Thompson, J. R. *et al*. Vortex pinning and slow creep in high-J_c MgB_2 thin films: a magnetic and transport study. *Supercond. Sci. Technol.* **18,** 970–976 (2005).
30. Reichhardt, C. & Reichhardt, C. J. O. Depinning and nonequilibrium dynamic phases of particle assemblies driven over random and ordered substrates: a review. *Rep. Prog. Phys.* **80,** 026501 (2017).
31. Pramanik, A. K. *et al*. Fishtail effect and vortex dynamics in LiFeAs single crystals. *Phys. Rev. B* **83,** 094502 (2011).
32. Zhou, W., Xing, X., Wu, W., Zhao, H. & Shi, Z. Second magnetization peak effect, vortex dynamics, and flux pinning in 112-type superconductor $Ca_{0.8}La_{0.2}Fe_{1-x}Co_xAs_2$. *Sci. Rep.* **6,** 22278 (2016).
33. Eley, S. *et al*. Decoupling and tuning competing effects of different types of defects on flux creep in irradiated $YBa_2Cu_3O_{7-\delta}$ coated conductors. *Supercond. Sci. Technol.* **30,** 015010 (2017).

Acknowledgements

This work was funded by the US DOE, Office of Basic Energy Sciences, Materials Sciences and Engineering Division (S.E., B.M. and L.C.). Sample fabrication was supported by the Japan Society for the Promotion of Science through the 'Funding Program for World-Leading Innovation R&D on Science and Technology'. M.M. was supported by JSPS KAKENHI (26709076).

Author contributions

S.E. carried out the magnetization measurements, data analysis, and assisted with theoretical analysis. L.C. and B.M. designed the experiment, and L.C. spearheaded the theoretical analysis. S.E. and L.C. wrote the manuscript. M.M. grew and performed microstructural characterization on the films. All authors participated in editing the manuscript.

Additional information

Supplementary information is available in the online version of the paper. Reprints and permissions information is available online at www.nature.com/reprints. Correspondence and requests for materials should be addressed to S.E.

Competing financial interests

The authors declare no competing financial interests.

Methods

Film growth and characterization. We used the film growth procedures reported previously[13]. Epitaxial films (80 nm thick) were deposited on MgO (100) single-crystalline substrates, held at 800 °C, by ablating pulsed laser deposition targets using the second harmonic (wavelength: 532 nm) of a pulsed Nd:YAG laser at a repetition rate of 10 Hz in vacuum of 10^{-4} Pa. Targets of nominal composition $BaFe_2(As_{0.67}P_{0.33})_2$ and $BaFe_2(As_{0.67}P_{0.33})_2 + 3$ mol% $BaZrO_3$ (BZO) were made by sintering Ba metal (99.99%, chunk), Fe metal (99.9%, no. 300 mesh pass), As powder (99.9999%, ~3 μm mm grain) and P powder (99.999%, no. 600 mesh pass). Mixtures of 1:1 Ba/As and $FeAs_{0.17}P_{0.33}$ were each separately heat treated in evacuated quartz tubes at 500 °C for 10 h and 650 °C for 20 h. The products were powdered and reacted at 650 °C for 10 h and 900 °C for 24 h. $BaZrO_3$ powder (3 mol%) was added to the resulting $BaFe_2(As_{0.67}P_{0.33})_2$ powder and reacted at 1,000 °C for 24 h to prepare the target with $BaZrO_3$. Transmission electron microscopy was used to analyse the microstructure and measure the film thickness. Energy dispersive X-ray spectroscopy and high-resolution transmission electron microscopy revealed stacking faults around the BZO inclusions[13].

Magnetization measurements. Magnetization studies were performed using a Quantum Design SQUID magnetometer to determine the critical temperature, T_c, and characterize the temperature and field dependence of J_c and S. The magnetization (M) was obtained by dividing the measured magnetic moment (m) by the sample volume $V = \delta wl$, where $\delta = 80$ nm is the film thickness, and $w \approx l \approx 3.5$ mm specifies sample width and length. Measurements of the Meissner slope confirmed that the superconducting volume was equivalent to the sample dimensions. For all measurements, the magnetic field was applied parallel to the c axis (perpendicular to the film plane). T_c was determined from magnetization as a function of temperature at $\mu_0 H = 0.001$ T. The critical current was calculated using the Bean critical-state model[34,35], $J_c = 20\Delta M/[w(1-(w/3l))]$, where ΔM is the difference between the upper and lower branches of isothermal magnetization loops $M(H)$.

Creep data were taken by using standard methods[36] for measuring the time-dependent magnetization, $M(t)$. First, the critical state was established by sweeping the field $\Delta H > 4H^*$, where H^* is the minimum field at which magnetic flux will fully penetrate the sample. Magnetization is then recorded every ~15 s; a brief measurement in the lower branch is collected to determine the background, and then the upper branch is measured as a function of time (t) for an hour fixed at the specified field. After subtracting the background and adjusting the time to account for the difference between the initial application of the field and the first measurement (maximize correlation coefficient), $S = -d\ln M/d\ln t$ is extracted from the slope of a linear fit to $\ln M$-$\ln t$.

Data availability. The data supporting Fig. 4 are available in the Supplementary Information file. All other data that support plots within this paper and other findings of this study are available from the corresponding author (S.E.) on request.

References

34. Bean, C. P. Magnetization of high-field superconductors. *Rev. Mod. Phys.* **36,** 31–39 (1964).
35. Gyorgy, E. M., Van Dover, R. B., Jackson, K. A., Schneemeyer, L. F. & Waszczak, J. V. Anisotropic critical currents in $Ba_2YCu_3O_7$ analyzed using an extended Bean model. *Appl. Phys. Lett.* **55,** 283–285 (1989).
36. Yeshurun, Y., Malozemoff, A. P. & Shaulov, A. Magnetic relaxation in high-temperature superconductors. *Rev. Mod. Phys.* **68,** 911–949 (1996).